Research Article Vol. 30, No. 14 / 4 Jul 2022 / *Optics Express* 25612

Optics EXPRESS

Focus-engineered sub-diffraction imaging in infrared-sensitive third-order sum frequency generation microscope

JYOTHSNA KONKADA MANATTAYIL,[1] LAL KRISHNA A. S.,[1] RABINDRA BISWAS,[1] HYUNMIN KIM,[2] AND VARUN RAGHUNATHAN[1,*]

[1] *Department of Electrical Communication Engineering, Indian Institute of Science, Bengaluru 560012, India*
[2] *Department of Interdisciplinary Engineering, DGIST, Daegu 42988, Republic of Korea*
[*] *varunr@iisc.ac.in*

Abstract: We experimentally demonstrate sub-diffraction imaging in infrared-sensitive third-order sum frequency generation (TSFG) microscope using focal-field engineering technique. The TSFG interaction studied here makes use of two mid infrared photons and a single 1040 nm pump photon to generate up-converted visible photons. Focal field engineering scheme is implemented using a Toraldo-style single annular phase mask imprinted on the 1040 nm beam using a spatial light modulator. The effect of focal field engineered excitation beam on the non-resonant-TSFG process is studied by imaging isolated silicon sub-micron disks and periodic grating structures. Maximum reduction in the measured TSFG central-lobe size by ~43% with energy in the central lobe of 35% is observed in the presence of phase mask. Maximum contrast improvement of 30% is observed for periodic grating structures. Furthermore, to validate the infrared sensitivity of the focus engineered TSFG microscope, we demonstrate imaging of amorphous Germanium-based guided-mode resonance structures, and polystyrene latex beads probed near the O-H vibrational region. We also demonstrate the utility of the focus engineered TSFG microscope for high resolution imaging of two-dimensional layered material. Focus-engineered TSFG process is a promising imaging modality that combines infrared selectivity with improved resolution and contrast, making it suitable for nanostructure and surface layer imaging.

1. Introduction

Improving the diffraction limited imaging performance of optical microscopes to visualize sub-wavelength objects at their native spatial scales has been an actively pursued area of research [1]. In addition to the use of high numerical aperture (NA) optics to improve the diffraction-limited resolution [2], techniques such as single molecule localization [3,4], structured illumination [5], and stimulated emission depletion (STED) [6] microscopy utilizing the properties of the fluorophores to achieve super-resolution have gained widespread adoption. Post processing of low-resolution images using Bayesian estimation technique [7], and deep learning [8] are also promising techniques to achieve super resolution. Though good advancements have been made in fluorescence microscopy, concerns with photo-bleaching and photo-toxicity limit the applicability of these techniques to any general imaging scenarios, thus motivating research into label-free nonlinear optical microscopy techniques. Techniques based on second harmonic generation (SHG) [9], third harmonic generation (THG) [10], sum frequency generation (SFG) [11–15], coherent anti-stokes Raman scattering (CARS) [16], and stimulated Raman scattering (SRS) [17] are some of the well-established imaging modalities. The multiphoton nature of the nonlinear imaging techniques improves spatial resolution when compared to the excitation wavelength, with inherent sectioning capability and improved damage tolerance [18]. Nonetheless, the

#459620 https://doi.org/10.1364/OE.459620
Journal © 2022 Received 30 Mar 2022; revised 7 Jun 2022; accepted 7 Jun 2022; published 30 Jun 2022

label-free nature of the signal generation makes it challenging to implement super-resolution techniques applicable to any generic sample of interest. Some of the super-resolution techniques implemented in nonlinear optical microscopy include the use of pupil plane phase masks for focal field engineering [19–24], spatial frequency modulation imaging [25,26], nonlinear structured illumination [27,28], and selective saturation of nonlinear optical processes [29–33]. The focus of the present work is on implementing focal field engineering technique in a third-order sum-frequency generation (TSFG) microscope. Using Toraldo-style pupil phase masks, the point-spread function is reshaped to create a narrow central-lobe with energy redistributed to the side-lobes along the transverse and longitudinal axes. The multiplicative effect of nonlinear optical processes with a second excitation beam without focal field shaping helps in attenuating the side-lobes, making this technique useful for sub-diffraction imaging. Such focal field engineered nonlinear imaging technique is generally applicable to any sample when compared to saturation-based techniques requiring certain intensity thresholds or specific sample properties to result in signal saturation. Nonetheless, the reduced energy in the central-lobe which can potentially lower the signal-to-noise ratio in the image and the trade-off between central-lobe size and energy in the side-lobes are outstanding challenges that need to be addressed for the focal-field engineering technique to gain wider applicability.

Infrared-sensitive TSFG studied here is a third-order nonlinear-optical process that offers chemical-specificity of infrared spectroscopy combined with improved resolution and detection sensitivity of up-converted visible photons. Unlike the second-order SFG process [10], the TSFG process can be observed in any sample without the requirement of non-centrosymmetry. Previous work on infrared sensitive TSFG microscopy reported diffraction-limited optical resolution of 450 nm for the process combining single photon of mid infrared (mid-IR) with two photons of near infrared (near-IR) [14]. Further improvement to the imaging resolution can enable visualization of the samples of interest in greater detail. Previous reports of super-resolution mid-IR microscopy have utilized photothermal [34], photoacoustic processes [35] and in combination with atomic force microscopy [36]. Here, we make use of a spatial light modulator (SLM) to generate programmable annular phase mask to achieve focal-field engineered sub-diffraction infrared-sensitive TSFG imaging. Focal field simulation studies incorporating the effect of central obscuration of the reflective objective is performed to quantify the expected resolution and contrast improvement. The resolution and contrast improvement are experimentally characterized by imaging silicon-based isolated nano-disks and periodic grating structures. The resonant TSFG process in combination with focus engineering imaging are further validated by imaging polystyrene bead and amorphous Germanium (a-Ge) sub-wavelength resonant gratings. We also report non-resonant TSFG imaging of 2D layered material with improved edge resolution and contrast.

2. Experimental setup

The nonlinear microscopy setup used for TSFG imaging is shown in Fig. 1(a). A femtosecond fiber laser at 1040 nm with 140 fs pulse width and 80 MHz repetition rate is used as the pump excitation (denoted by ω_p). A portion of the pump laser is used to synchronously pump an optical parametric oscillator (OPO) to generate the mid-IR beam in the range of 2600-3600 nm, with pulse-width of 200 fs and 80 MHz repetition rate (denoted by ω_i). The pump and mid-IR beams are combined using a dichroic beam combiner to overlap them temporally and spatially. The beams are focused using a reflective objective of 0.65 numerical aperture (NA) (Beck Optronics, part no. 5007). The Schwartzchild reflective objective ensures achromatic focusing of the pump and infrared beams on to the sample, albeit with a central obscuration blocking a fraction of the incident light [37]. The TSFG signal (denoted by $\omega_{TSFG} = \omega_p + 2\omega_i$) generated from the sample placed in an inverted microscope setup (Olympus IX73) is collected in the epi-direction and detected using a photomultiplier tube (PMT, Hamamatsu R3896). TSFG images are obtained by scanning the sample placed on a XY stage (Thorlabs, MLS203-1) and Z-scanning by utilizing a motor connected to the focus knob (Prior Scientific, PS3H122R). Beam shaping of the 1040 nm laser is done using a spatial light modulator (Holoeye, PLUTO-2-NIR-011 [38]). A single-phase step Toraldo-style phase mask with 0-π phase step with varying mask diameters is projected on the SLM, as shown in the inset of Fig. 1(a). The phase shaped beam is imaged on to the back aperture of the reflective objective using two 4-f imaging systems. The first 4-f lens pair consisting of glass lenses of 50 cm focal length are used in the 1040 nm beam path to image the SLM plane close to the dichroic and a second pair of CaF_2 lenses of focal length 50 cm are used in the common path of pump and infrared beam to project the image onto the back aperture of the objective.

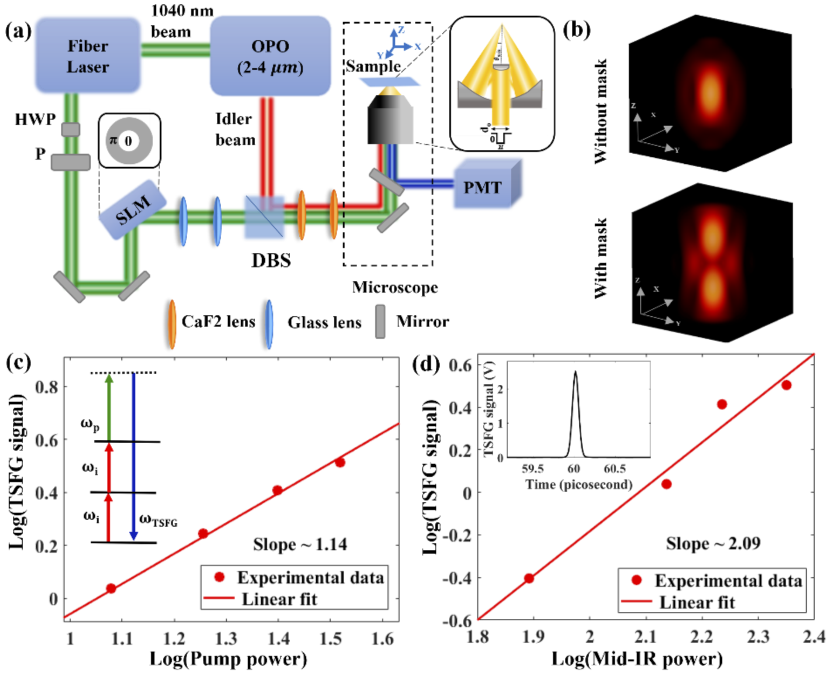

Fig. 1. (a) Schematic of the TSFG microscope setup. HWP: Half waveplate, P: Polarizer, DBS: Dichroic beam splitter, SLM: Spatial light modulator, PMT: Photomultiplier tube. Annular phase mask and the schematic of the reflective objective used are shown as inset in figure (a). (b) Three-dimensional point spread function at 1040 nm without and with phase mask. Power dependence of the nonlinear signal as a function of increasing power for: (c) pump beam, ω_P, and (d) mid-IR beam, ω_i. The inset to figures (c) and (d) show the energy diagram of TSFG process and the time dependence of TSFG signal as a function of varying delay between pump and infrared input pulses, respectively.

Figure 1(b) shows representative three-dimensional point spread function (PSF) without and with phase mask for the incident pump beam at 1040 nm. Inset in Fig. 1(c) shows the energy diagram representation of the TSFG process studied in this work. One photon of pump and two photons of the mid-IR are combined to give the TSFG signal. The TSFG signal can also be generated using two photons of pump and one photon of mid-IR. The former TSFG process is studied in this work due to the incident power limitation for the SLM used for phase shaping of the pump beam [14]. The preliminary characterization of the TSFG microscope to optimize the temporal, spatial overlap, and the dependence of the TSFG signal on the incident laser power are discussed below. A uniform film of amorphous Silicon (a-Si) is used for this purpose giving strong non-resonant TSFG signal. Figures 1(c) and (d) show the TSFG signal measured at varying incident power levels. The slopes of the two power dependence plots (shown as log-log plot) obtained as 1.14 and 2.09 with respect to the pump and mid-IR beams respectively, confirming that the nonlinear signal generated is from the TSFG process of interest. The inset of Fig. 1(d) shows the TSFG signal measured as a function of varying temporal delay between the pump and the mid-IR beam, confirming the strong signal obtained due to the interaction of the pump and mid-IR beams.

3. Focal field simulations

To study the effect of phase mask on the PSF of the TSFG microscope, we theoretically model the three-dimensional vectorial fields generated at the focus of the focusing optics, *E(x,y,z)* using angular spectrum representation [19,20]. The focal fields are calculated as follows:

$$\begin{gathered} E(x,y,z) = \frac{if}{\lambda} e^{-ikf} \int_0^{\theta_{max}} d\theta \int_0^{2\pi} d\phi \left(\frac{n_1}{n_2}\right)^{\frac{1}{2}} X\ sin\theta\sqrt{cos\theta}\cdot \\ \cdot\ e^{ik(xsin\theta cos\phi+ysin\theta sin\phi+zcos\theta)} X\ R_\phi^{-1} R_\theta^{-1} R_\phi E_{inc} \end{gathered} \tag{1}$$

$$R_\phi = \begin{bmatrix} cos\phi & sin\phi & 0 \\ -sin\phi & cos\phi & 0 \\ 0 & 0 & 1 \end{bmatrix} R_\theta = \begin{bmatrix} cos\theta & 0 & -sin\theta \\ 0 & 1 & 0 \\ sin\theta & 0 & cos\theta \end{bmatrix} \tag{2}$$

Unlike refractive objectives that use lenses to focus light, the Schwarzschild reflective objective utilizes two curved mirrors to focus light. This curved mirror-based focusing provides several advantages, such as broad wavelength range operation and achromatic performance, making it attractive for use in infrared up-conversion experiments. However, the design of mirror assembly and spider veins to hold the central mirror results in a central obscuration which sets a non-zero lower limit to the supported angular span [37]. This central obscuration of the reflective objective is modeled in the simulations performed here by defining the incident field for reflective objective as E_{inc} as follows:

$$E_{inc} = \begin{cases} 0\ , & 0<\theta<\ \theta_{min} \\ E_{input}\ , & \theta_{min} \le \theta \le\ \ \theta_{max} \end{cases} \tag{3}$$

where θ_{max} corresponds to maximum collection angle of the reflective objective and θ_{min} corresponds to the maximum angle of obscuration which is proportional to square root of the obscuration area [37]. For the reflective objective used here with central area obscuration of 13.3, the angular span supported for the focused beam is obtained as 14 to 40°. It is emphasized that an exact calculation of the focal fields for the reflective objective requires treatment of wavefront reflection from the two curved mirrors. Previous reports have made use of ray-tracing models in Zemax software to visualize the focal fields of a reflective objective [39,40]. The angular spectrum representation considered in this work using spherical wavefront is known to be best suited for computing vectorial fields obtained from high numerical objectives [19,20]. It is a good approximation of the focal fields for a reflective objective, as supported by the comparison between the simulations and experiments presented below.

The calculated focal field intensity ($|E|^2$) profiles at the excitation wavelengths are shown in Figs 2(a)-(d). The field profile corresponding to the 1040 nm pump beam in the absence of phase mask and in the presence of simulated phase masks of diameter $0.53d_o^s$ and $0.66d_o^s$ are shown in Figs. 2(a)-(c). Here, the full diameter of the pump beam at the back aperture of the objective in the simulation study is denoted by d_o^s. The mid-IR field profiles are shown in Fig. 2(d). The focal field profiles along transverse (XY, with $Z = 0$) and longitudinal (XZ, with $Y = 0$) planes are shown as indicated in the figures. The third-order nonlinear polarization for the TSFG process is calculated as follows [41]:

$$P^{(3)}(\omega_{TSFG}, r) = \varepsilon_0 \chi^{(3)}(\omega_{TSFG}, ; \omega_p, \omega_i, \omega_i)E_p(\omega_p, r)E_i(\omega_i, r)E_i(\omega_i, r) \tag{4}$$

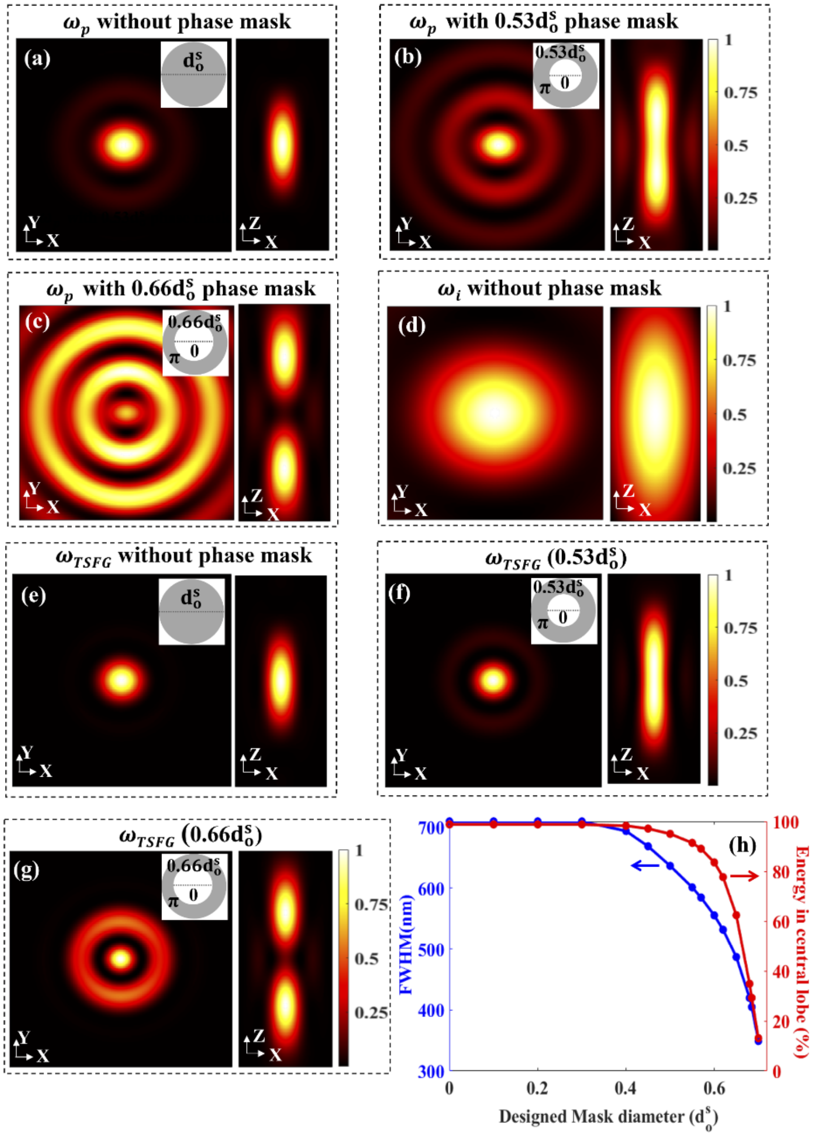

Fig. 2. Calculated focal field intensity, $|E|^2$ for pump beam: (a) without phase mask, (b) with $0.53d_o^s$ mask, (c) $0.66d_o^s$ mask, and (d) mid-IR beam without phase mask along both XY ($Z = 0$) and XZ ($Y = 0$) planes. The TSFG nonlinear polarization strength at the focus obtained along XY and XZ planes for the case: (e) without phase mask, (f) with $0.53d_o^s$ mask and (g) $0.66d_o^s$ mask are shown. Profiles are shown for transverse (XY – 5 × 5 µm) and longitudinal (XZ – 3 × 14 µm) planes. (h) Central-lobe FWHM - left axis and percentage of energy in the central-lobe - right axis are shown as a function of varying simulated phase mask diameters.

The corresponding nonlinear polarization profiles are shown in Figs. 2(e)-(g). With increasing phase mask diameter, narrowing of the central lobe and redistribution of the energy to the side-lobes both along the transverse and longitudinal axes are observed in Figs. 2(a)-(c). The side-lobes along the longitudinal axis are found to elongate in the presence of smaller phase mask diameter and subsequently split to prominent side-lobes. Such shaped beams have been used previously for optical trapping [42] and to enhance contrast along longitudinal interfaces [43]. The narrowed central-lobe can be utilized to improve imaging resolution; this however comes at the price of increased side-lobe strength, which can deteriorate the imaging performance both in the focal plane and along the axial direction. The focal field engineering scheme for resolution improvement often finds a compromise between the narrowing of the central-lobe and deterioration of imaging performance due to increased side-lobe strength. In the context of TSFG process, the quadratic dependence on the mid-IR field helps in spatial clean-up of the phase-shaped pump focal field to reduce side-lobe signal strength. As seen from the TSFG polarization profiles for the three cases considered above in Figs. 2(e)-(g), a clear reduction in the side-lobe strength is observed along the XY and XZ-planes. Figure 2(h) shows the effect of different phase mask diameters on the full-width at half-maximum - FWHM of the central lobe (blue curve – left axis) and percentage energy in the central lobe (red curve – right axis). The diffraction-limited resolution is calculated as ~700 nm in the absence of phase mask. The narrowing of central lobe and the side-lobe gaining in strength with increase in the mask diameter are clearly observed [19]. An optimum phase mask diameter of $0.66d_o^s$ results in maximum improvement in FWHM of 52% with 45% energy in the central-lobe for the TSFG process. The two photons of the mid-IR beam suppress the side-lobe strength of focus engineered beam in the transverse plane from 81% to 45% (~44% suppression) and the axial FWHM from 11.48 μm to 9.78 μm (~17% improvement) for $0.66d_o^s$ phase mask diameter.

4. Results and discussion

The resolution and contrast of the TSFG microscope are characterized using a patterned a-Si sample exhibiting non-resonant TSFG. Figure 3(a) shows a schematic of the a-Si structures used in this study. The a-Si samples are fabricated using standard silicon fabrication techniques. For resolution characterization, a 3×3 array of a-Si nano-disks of thickness 60 nm and 20 μm spacing, with diameter varying from 100 nm to 500 nm are used. For contrast characterization, a-Si one-dimensional gratings of thickness 60 nm, with pitch ranging from 20 μm to 500 nm are used. Figures 3(b) and (c) show the representative TSFG images of 500 nm diameter nano-disks and 10 μm grating pitch respectively. Figure 3(d) shows the PSF map for the TSFG process experimentally measured using an isolated 150 nm diameter a-Si nano-disk in the absence of any phase mask. The diffraction-limited resolution is estimated from the experimentally measured FWHM as 683 nm and 606 nm along the X and Y directions with ~91% energy in central lobe respectively for X-polarized pump and mid-IR incidence.

Figures 3(e)-(i) show the measured PSF for focal-field engineered TSFG microscope with phase masks of $0.37d_o$, $0.38d_o$, $0.41d_o$, $0.46d_o$ and $0.48d_o$ on the SLM, where d_o corresponds to the full diameter of the first mirror within the reflective objective, as used in the experiments. With the use of the above phase masks, a narrowing of the central lobe to 612 nm, 592 nm, 532 nm, 521 nm and 475 nm along X direction is observed with central-lobe energy percentage decreasing to ~77%, 71%, 75%, 65% and 35%, respectively. We observed a maximum narrowing of 43% in the FWHM of the central-lobe, with 35% energy in the central lobe. The difference between the simulated (d_o^s) and experimentally obtained (d_o) phase mask diameters for resolution improvement is attributed to the approximation of the reflective objective by a refractive curved surface with a central obscuration in the back-aperture to compute the focal fields. Good agreement is however seen in the central-lobe size and its energy content when comparing focal field simulations (Fig. 2(h)) and experiments (Fig. 3(j)), thus pointing to the accuracy of

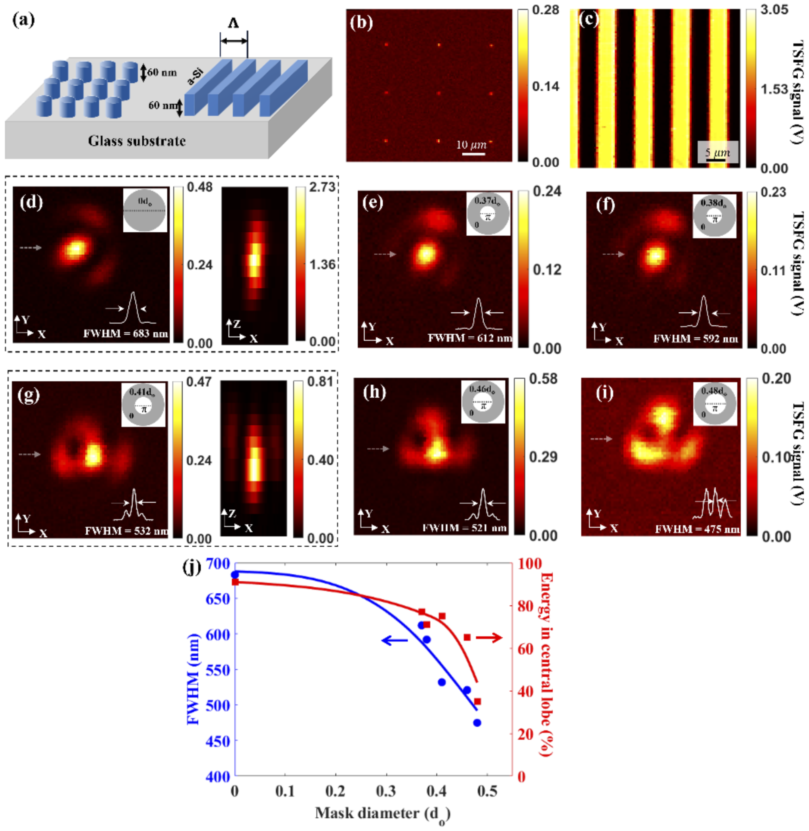

Fig. 3. (a) Schematic of the fabricated a-Si nano-disk array and gratings used for resolution and contrast characterization. Representative TSFG image of: (b) a-Si nanodisk array of 500 nm diameter, and (c) gratings with 10 μm pitch. TSFG focal fields obtained by scanning a 150 nm isolated a-Si nanodisk: (d) without phase mask along XY and XZ planes, (e) $0.37d_o$ mask along XY plane, (f) $0.38d_o$ mask along XY plane, (g) $0.41d_o$ mask along XY and XZ planes, (h) $0.46d_o$ mask along XY plane, and (i) $0.48d_o$ mask along XY plane. The schematic of the phase mask used and the FWHM measured from the line profile drawn along X direction (as indicated by the arrow) is shown in the inset. Profiles shown are of size: transverse (XY –5 × 5μm) and (XZ - 3 × 14 μm). (j) Experimentally measured central lobe FWHM - left axis and percentage of energy in the central-lobe - right axis are shown as a function of varying phase mask diameters.

the expected resolution improvement. The slight elongation observed in the nonlinear PSF in Fig. 3(d) and non-uniform energy distribution in the side-lobes in Figs. 3(h),(i) are attributed to misalignments between the primary and secondary mirrors inside the reflective objective causing distortions in the focal field. The absence of a circular side-lobe is attributed to the spider veins arrangement of the mirrors within the reflective objective thereby blocking a fraction of the focusing light.

Next, we characterized the contrast improvement by simulating and experimentally obtaining TSFG images of periodic grating structures. The far-field propagation of the nonlinear signal is calculated using Green's function integral of the TSFG nonlinear polarization at a far distance R as follows [20,44]:

$$E(\omega\mathrm{TSFG},\ \mathrm{R}) = -\int \frac{e^{ik|R-r|}(R-r)}{4\pi\,|R-r|^3} \times [(R-r) \times P(\omega\mathrm{TSFG},\ \mathrm{r})]d^3{}_r \tag{5}$$

The far-field TSFG signal obtained at the detector plane after integrating across the angular span of the reflective objective is given as:

$$I_{far} = \int_0^{2\pi} d\varphi \int_{\theta_{min}}^{\theta_{max}} d\theta R^2 \sin\theta |E(R,\theta,\varphi)|^2 \tag{6}$$

The TSFG imaging of periodic structure is modeled by scanning a thin 1D grating across the focal volume, computing the nonlinear polarization, and propagating it to the far-field for detection of the TSFG signal at the detector. The image contrast is computed as: $\left(\frac{I_{max}-I_{min}}{I_{max}+I_{min}}\right)$, where I_{max} and I_{min} corresponds to the maximum and minimum TSFG signals obtained across the grating structure.

Figures 4(a) and (b) show the experimentally obtained non-resonant TSFG images of the gratings across an area of 4.5×2.25 μm^2 in the absence and presence of phase mask of diameter 0.36d$_o$ respectively. Figures 4(c) and (d) show the comparison between simulated and experimentally obtained TSFG line-scan respectively for gratings of 900 nm pitch, in the absence and presence of phase mask. The simulated TSFG line scans show an overall contrast increase from 0.313 to 0.414 (~32% improvement). In comparison, the experimentally obtained TSFG lines scans show similar contrast increase from 0.291 and 0.377 (~30% improvement). Figures 4(e) and (f) show the measured contrast (filled data points) as a function of varying grating pitch in the absence and presence of phase mask with set mask diameter of 0.36d$_o$ respectively. For comparison, the contrast obtained from simulated TSFG line scans are also shown in the absence and phase masks of diameters 0.50d$_o^s$, 0.60d$_{o,}^s$0.65d$_o^s$ and 0.68d$_o^s$. Good agreement is obtained between the simulated and experimentally measured contrast both with and without the phase mask. Comparing the contrast with and without phase mask show improvement in contrast for lower grating pitch values (as indicated by the green shaded region in Figs. 4(e) and (f)). We also observe local maxima in the contrast plot for certain pitch values in the presence of phase mask in Fig. 4(f). This is attributed to the gratings being imaged using multi-lobed focus engineered beam resulting in periodic blocking and unblocking of the side lobes in the nonlinear PSF. This results in improvement in contrast when the multi-lobed focal field matches the grating pitch, thus amplifying certain spatial frequencies of the grating structure. With the use of higher mask diameter such as the 0.68d$_o^s$ case, we observe that the contrast drops to value close to zero at selected pitch sizes showing the deterioration of image quality in the presence of strong sidelobes. This further reiterates the point that the choice of the mask diameter is crucial while using this technique for resolution improvement.

To further demonstrate the practical utility of focal field engineered TSFG microscope, we image infrared resonant sub-wavelength grating structures, polystyrene beads and two-dimensional layered material. The sub-wavelength resonant gratings and polystyrene beads exhibit infrared sensitive resonant TSFG, while the 2D layered material samples exhibits non-resonant TSFG. In the experimental TSFG imaging studies discussed below, we restrict the phase mask profile to

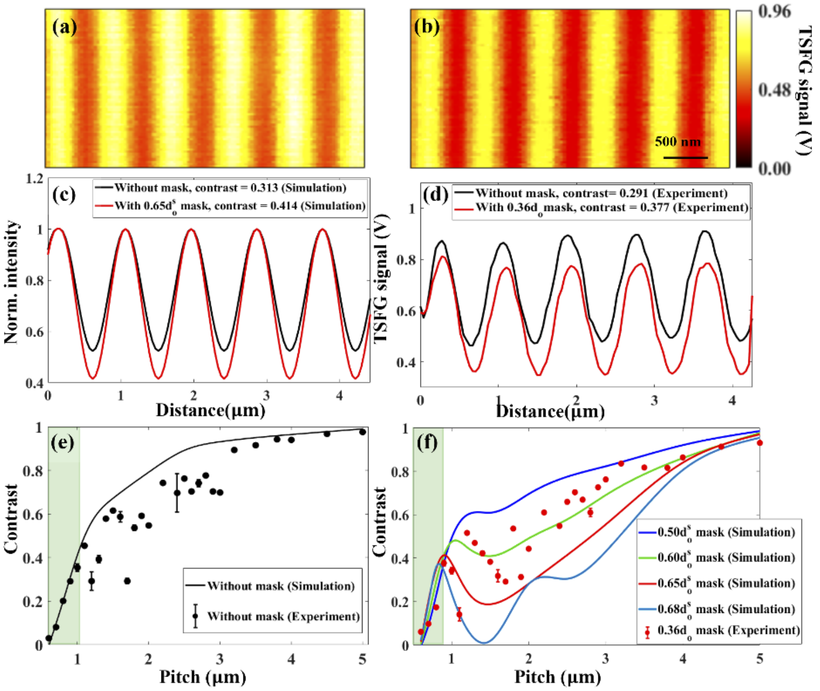

Fig. 4. TSFG image of a-Si grating of 900 nm pitch for the cases: (a) without, and (b) with phase mask of 0.36d_o diameter. (c) Comparison of the simulated TSFG line scans of the grating without and with phase mask. (d) Comparison of experimentally obtained TSFG line scans of the grating taken without and with phase mask. (e) Experimentally measured (black filled circles) and calculated (black curve) contrast of the TSFG line scans as a function of varying grating pitch without phase masks. (f) Experimentally measured (red filled circles) and calculated (blue, green, and red curves) contrast of the TSFG line scans as a function of varying grating pitch with phase masks. The range of pitch values where improvement in contrast is observed is indicated by the green shaded region.

less than 0.41d_o, to reach a good balance between the achievable resolution/ contrast and the percentage of energy in the side-lobe in the XY plane. The resonant structure utilized here consist of a-Ge one dimensional sub-wavelength gratings on quartz substrate supporting guided-mode resonances in the mid-IR wavelength range [45]. Figure 5(a) shows an optical image of the a-Ge grating sample, with the corresponding scanning electron microscopy (SEM) image shown as an inset. The dimensions of the sub-wavelength gratings are pitch, $\Lambda = 2.1$ µm, duty cycle = 50%, film thickness = 460 nm and grating etch depth of ~210 nm. The reflection spectrum from the gratings measured using a Fourier-transform infrared spectrometer (FTIR) is shown in Fig. 5(b) - left axis. Clear resonance is observed in the transmission spectrum at a wavelength of ~3295 nm. This is attributed to the excitation of guided-mode resonances within the sub-wavelength, partially etched a-Ge structures due to the wavelength selective in- and out-coupling of light into the a-Ge un-etched layer in the presence of the sub-wavelength gratings [45].

For TSFG studies, the mid-IR beam is tuned in the range of 2700 - 3600 nm and the TSFG signal selectively detected using two band-pass filters (605 nm ± 27.5 nm and 650 nm ± 20 nm) in front of the PMT. The TSFG spectrum obtained from the a-Ge gratings is also shown in Fig. 5(b) - right axis. The TSFG signal is found to reach a maximum at ~3325 nm in close vicinity to the resonance dip observed in the reflection spectrum. The broadening of the TSFG spectrum when compared to the linear reflection spectrum is attributed to the broader spectral

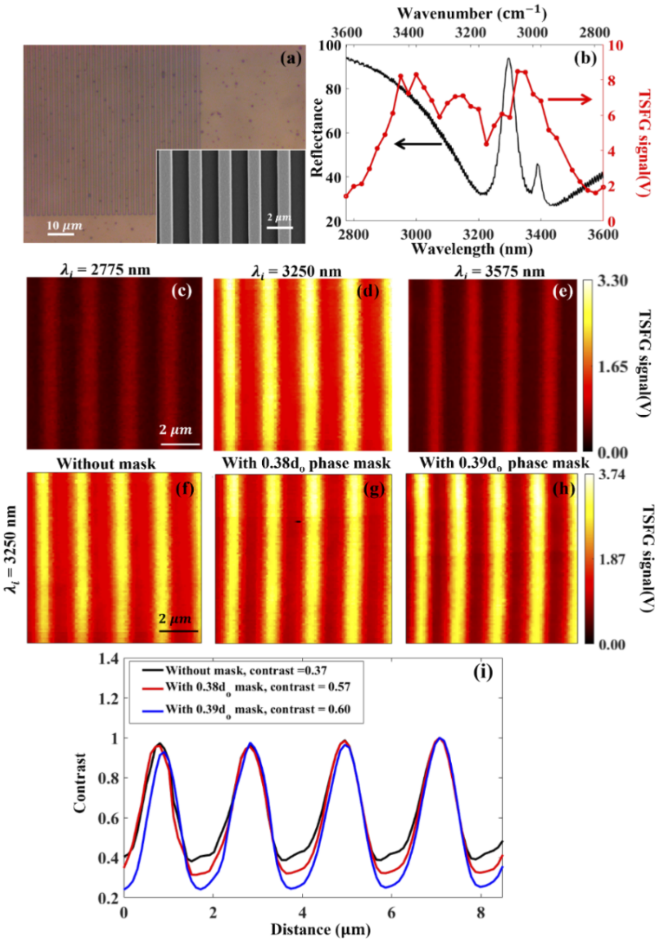

Fig. 5. (a) Optical image of the a-Ge sub-wavelength gratings used for TSFG studies. SEM image of the gratings is shown as an inset. (b) Linear reflectance spectra of the fabricated a-Ge sub-wavelength gratings - left axis and TSFG spectrum as a function of varying mid-IR wavelengths - right axis. TSFG image of the a-Ge sub-wavelength grating obtained for mid-IR wavelength of: (c) 2775 nm, (d) 3250 nm, and (e) 3575 nm. TSFG images obtained at 3250 nm mid-IR wavelength: (f) without phase mask, (g) 0.38d$_o$ phase mask, and (h) 0.39d$_o$ phase mask. (i) Line scans obtained from the TSFG images without and with phase mask.

width mid-IR source combined with the wider angular excitation of the grating structures in the TSFG experiments. TSFG images obtained corresponding to the mid-IR wavelengths of 2775 nm, 3250 nm and 3575 nm are shown in Figs. 5(c)-(e). The TSFG image contrast is found to follow the TSFG signal spectrum with the best contrast obtained for 3250 nm excitation. The grating structures are also imaged using phase shaped pump excitation close to the resonance wavelength at 3250 nm. A comparison of grating images taken without phase mask, and with phase mask of $0.38d_o$ and $0.39d_o$ are shown in Figs. 5(f)-(h) respectively. The corresponding line scans are shown in Fig. 5(i). As seen from the line scan profiles, the grating image contrast increases from 0.37 without phase mask to 0.57 and 0.60 in the presence of phase masks of diameter $0.38d_o$ and $0.39d_o$, respectively. Clear improvement in imaging contrast combined with infrared sensitivity is observed when utilizing focus engineered TSFG microscopy for imaging such periodic structures.

Polystyrene beads (PS) of diameter 3 µm (Sigma Aldrich, LB30) and 0.6 µm (Sigma Aldrich, LB06) prepared by drop-casting diluted bead suspension (1:10 in DI water) and drying in air are used for TSFG imaging. Here we focus on imaging with the mid-IR excitation tuned to the O-H vibrational modes due to the strong TSFG signal obtained in the O-H region when compared to the C-H region when using femtosecond pump and mid-IR excitation sources. Figure 6(a) shows the spectral dependence of TSFG images obtained from 3 µm diameter beads showing strong TSFG signal for the mid-IR beam tuned to 3050 nm to probe the O-H vibration bond in the sample. The TSFG signal is detected using a band-pass filter (605 nm ± 27.5 nm). The TSFG images corresponding to mid-IR excitation at 2850 nm and 3050 nm are shown in Figs. 6(b) and (c) respectively, with clear enhancement in contrast observed corresponding to the O-H peak at 3050 nm. Further, to study the effect of focus engineering for resolution improvement, we image polystyrene beads of 0.6 µm diameter for mid-IR excitation at 3050 nm. TSFG image of polystyrene bead obtained in the absence and presence of phase mask of diameter $0.38d_o$ are shown in Figs. 6(d) and (e). This is also shown in the line scan plots in Figs. 6(f)-(i) across locations 1, 2, 3 and 4 respectively, as indicated in the TSFG images. The images acquired with focus engineered TSFG clearly shows improvement in contrast, that helps in resolving closely spaced PS beads when compared to the one without the phase mask.

Second-order SFG microscopy has been widely used for surface imaging of films to study the molecular orientation and dynamics of the interfacial material [46]. Here, we use the focus engineered non-resonant TSFG for imaging thin 2D material flakes with improved resolution and contrast. Nonlinear optical micro-spectroscopy is a promising technique for 2D material characterization to understand crystal orientation, layer stacking and defects [47]. Figure 7(a) shows the optical image of multilayer Tin diselenide ($SnSe_2$) flake used in this study. $SnSe_2$ is a well-known 2D material with strong second- and third-order nonlinear optical properties [48,49]. Figures 7(b) and (c) show the TSFG image taken without any phase mask and with phase mask of diameter $0.38d_o$ respectively. The non-resonant TSFG images are obtained using mid-IR excitation at 3000 nm along with the pump excitation at 1040 nm, with the corresponding TSFG signal at 615 nm collected using a band-pass filter (605 nm ± 27.5 nm). Comparison of line scan profiles corresponding to the regions marked 1, 2 and 3 are shown in Figs. 7(d)-(f). Figure 7(d) clearly shows improvement in edge contrast in the presence of the phase mask. Figure 7(e) shows better contrast in resolving TSFG signal from $SnSe_2$ regions of different thicknesses in the presence of phase mask. Figure 7(f) further shows improved contrast and gap resolution in the presence of phase mask.

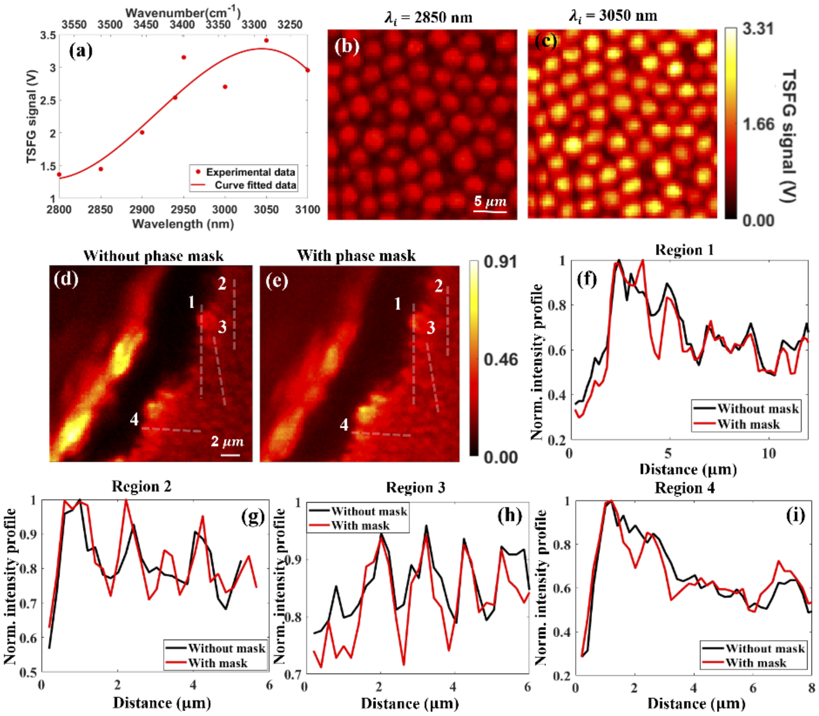

Fig. 6. (a) TSFG spectrum obtained from 3 µm size polystyrene beads. TSFG image of the polystyrene beads at wavelength of: (b) 2850 nm, and (c) 3050 nm. TSFG image of 0.6 µm polystyrene beads imaged: (d) without, and (e) with phase mask of 0.38d$_o$ diameter. (f)-(i) Line profile of regions marked 1, 2, 3, and 4, respectively.

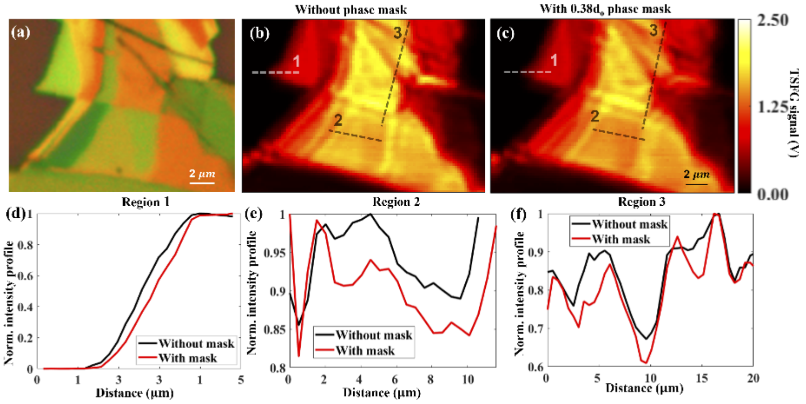

Fig. 7. (a) Optical image of the SnSe$_2$ flake on glass substrate. (b) TSFG image of SnSe$_2$ flake acquired without phase mask. (c) TSFG image of SnSe$_2$ flake with 0.38d$_o$ diameter phase mask. (d)-(f) TSFG line scan profile across regions marked as 1, 2, and 3 in the TSFG image taken without mask (black line) and with phase mask of 0.38d$_o$ diameter (red line).

5. Conclusions

The infrared sensitive TSFG process results in up-conversion of mid-IR information to the visible wavelength range offering the benefits of improved spatial resolution and detection efficiency when compared to direct IR absorption-based imaging. Further improvement in optical resolution for the TSFG process is useful in resolving samples with improved spatial details. In this context, using focal field calculations and experimental results we have demonstrated sub-diffraction imaging capability for focus-engineered infrared sensitive TSFG microscopy. Toraldo-type pupil phase masks with single concentric 0-π phase step with varying mask diameter are utilized to shape the focal field profile for the pump beam at 1040 nm. The effect of the phase engineered incident excitation on the TSFG resolution and contrast properties are characterized by imaging silicon-based isolated nano-disks and periodic grating structures. The focus engineered TSFG microscope results in best improvement of 43% in central-lobe FWHM with 35% energy in the central-lobe and 30% contrast improvement when compared to the conventional TSFG microscope. The utility of the focal-field engineering technique for contrast enhancement in infrared sensitive TSFG microscope is demonstrated by imaging germanium-based resonant grating structures and polystyrene beads. We have also demonstrated the application of focus engineered TSFG microscope for surface imaging of 2D layered materials. $SnSe_2$ flakes are imaged using TSFG microscopy exhibiting enhanced contrast, edge and gap resolution with the focus engineered excitation beam. The presence of prominent sidelobes along the optical axis deteriorates the axial resolution with the use of annular phase masks and limits the utility of super-resolution imaging for three-dimensional imaging. The technique studied here is potentially useful for single-plane imaging of nanostructure or thin film samples.

The focus engineered TSFG process studied in this work utilizes two photons in the mid-IR and one pump photon in the near infrared to generate TSFG signals in the 600-700 nm wavelength range. TSFG process can be generated using two photons of near-IR and one photon of mid-IR with TSFG signal generated at shorter wavelengths in the range of 400-500 nm. It is pointed out that the focus-engineering scheme demonstrated here is general and applicable to the other TSFG process with similar improvements expected for resolution and contrast. The focus engineered TSFG process is a promising imaging modality that combines infrared selectivity with improved resolution and contrast for nanostructures and surface layer imaging.

Funding. Department of Science and Technology, Ministry of Science and Technology, India (Indo-Korea Joint Research Project - INT/Korea/P-44); Science and Engineering Research Board (Core Research Grant).

Disclosures. The authors declare no conflicts of interest.

Data availability. Data underlying the results presented in this paper are not publicly available at this time but may be obtained from the authors upon reasonable request.

References

1. L. Schermelleh, R. Heintzmann, and H. Leonhardt, “A guide to super-resolution fluorescence microscopy,” J. Cell Biol. **190**(2), 165–175 (2010).
2. W. Lukosz, “Optical systems with resolving powers exceeding the classical limit,” J. Opt. Soc. Am. **56**(11), 1463–1471 (1966).
3. M. A. Thompson, M. D Lew, and W. E. Moerner, “Extending microscopic resolution with single-molecule imaging and active control,” Annu. Rev. Biophys. **41**(1), 321–342 (2012).
4. E. Betzig, G. H. Patterson, R. Sougrat, O. W. Lindwasser, S. Olenych, J. S. Bonifacino, M. W. Davidson, J. Lippincott-Schwartz, and H. F. Hess, “Imaging intracellular fluorescent proteins at nanometer resolution,” Science **313**(5793), 1642–1645 (2006).
5. B. R. Masters, “Structured Illumination Microscopy,” Springer Ser. Opt. Sci **227**, 233–260 (2020).
6. B. Harke, J. Keller, C. K. Ullal, V. Westphal, A. Schönle, and S. W. Hell, “Resolution scaling in STED microscopy,” Opt. Express **16**(6), 4154–4162 (2008).
7. S. Omatu and H. Araki, “Image Restoration by Revised Bayesian-Based Iterative Method,” in *Fifth International Conference on Advanced Engineering Computing and Applications in Sciences* 60–65 (IARIA, 2011).
8. H. Wang, Y. Rivenson, Y Jin, Z. Wei, R. Gao, H. Günaydın, L.A. Bentolila, C. Kural, and A. Ozcan, “Deep learning enables cross-modality super-resolution in fluorescence microscopy,” Nat. Methods **16**(1), 103–110 (2019).

9. X. Chen, O. Nadiarynkh, S. Plotnikov, and P. J. Campagnola, “Second harmonic generation microscopy for quantitative analysis of collagen fibrillar structure,” Nat. Protoc. **7**(4), 654–669 (2012).
10. M. A. Laire, S. C. Lein, C. H. S. Tringari, and E. M. B. Eaurepaire, “High-speed polarization-resolved third-harmonic microscopy,” Optica **6**(3), 385–388 (2019).
11. V. Raghunathan, Y. Han, O. Korth, N.H. Ge, and E. O. Potma, “Rapid vibrational imaging with sum frequency generation microscopy,” Opt. Lett. **36**(19), 3891–3893 (2011).
12. Y. Han, V. Raghunathan, R.R. Feng, H. Maekawa, C. Y. Chung, Y. Feng, E.O. Potma, and N.H Ge, “Mapping molecular orientation with phase sensitive vibrationally resonant sum-frequency generation microscopy,” J. Phys. Chem. B **117**(20), 6149–6156 (2013).
13. Y. Han, J. Hsu, N. H. Ge, and E. O. Potma, “Polarization-sensitive sum-frequency generation microscopy of collagen fibers,” J. Phys. Chem. B **119**(8), 3356–3365 (2015).
14. A. M. Hanninen, R. C. Prince, R. Ramos, M. V. Plikus, and E. O. Potma, “High-resolution infrared imaging of biological samples with third-order sum-frequency generation microscopy,” Biomed. Opt. Express **9**(10), 4807–4817 (2018).
15. K. Kuhnke, D. M. Hoffmann, X. C. Wu, A. M. Bittner, and K. Kern, “Chemical imaging of interfaces by sum-frequency generation microscopy: Application to patterned self-assembled monolayers,” Appl. Phys. Lett. **83**(18), 3830–3832 (2003).
16. J.-X. Cheng and X. S. Xie, *Coherent Raman Scattering Microscopy* (CRC, 2016).
17. C. W. Freudiger, W. Min, B. G. Saar, S. Lu, G. R. Holtom, C. He, J. C. Tsai, J. X. Kang, and X.S. Xie, “Label-free biomedical imaging with high sensitivity by stimulated Raman scattering microscopy,” Science **322**(5909), 1857–1861 (2008).
18. B. R. Masters and P. So, *Handbook of Biomedical Nonlinear Optical Microscopy* (Oxford University, 2008).
19. Vishnu Vardhan Krishnamachari and E. O. Potma, “Focus-engineered coherent anti-Stokes Raman scattering microscopy: a numerical investigation,” J. Opt. Soc. Am. A **24**(4), 1138–1147 (2007).
20. V. Raghunathan and E. O. Potma, “Multiplicative and subtractive focal volume engineering in coherent Raman microscopy,” J. Opt. Soc. Am. A **27**(11), 2365–2374 (2010).
21. H. Kim, G. W. Bryant, and S. J. Stranick, “Superresolution four-wave mixing microscopy,” Opt. Express **20**(6), 6042–6051 (2012).
22. R. Beams, J. W. Woodcock, J. W. Gilman, and S. J. Stranick, “Phase mask-based multimodal superresolution microscopy,” Photonics **4**(4), 39 (2017).
23. L. Gong, J. Lin, C. Hao, W. Zheng, S.Q.Y Wu, J. Teng, C. W. Qiu, and Z. Huang, “Supercritical focusing coherent anti-Stokes Raman scattering microscopy for high-resolution vibrational imaging,” Opt. Lett. **43**(22), 5615–5618 (2018).
24. A. Fathi, C. Y. Chung, Y. P. Lee, and E. W. G. Diau, “Label-Free Optical Microscope Based on a Phase-Modulated Femtosecond Pump-Probe Approach with Subdiffraction Resolution,” ACS Photonics **7**(3), 607–613 (2020).
25. J. J. Field, K. A. Wernsing, S. R. Domingue, A. M. A. Motz, K. F. DeLuca, D. H. Levi, J. G. DeLuca, M. D. Young, J. A. Squier, and Bartels, “Superresolved multiphoton microscopy with spatial frequency-modulated imaging,” Proc. Natl. Acad. Sci. U. S. A. **113**(24), 6605–6610 (2016).
26. S. Heuke, S. Sivankutty, C. Scotte, P. Stockton, R.A Bartels, A. Sentenac, and H. Rigneault, “Spatial frequency modulated imaging in coherent anti-Stokes Raman microscopy,” Optica **7**(5), 417–424 (2020).
27. M. J. Huttunen, A. Abbas, J. Upham, and R. W. Boyd, “Label-Free Super-Resolution Microscopy with Coherent Nonlinear Structured-Illumination,” *20th International Conference on Transparent Optical Networks*, 085504 (2018).
28. C. H. Yeh, C. Z. Tan, C. A Cheng, J. T. Hung, and S. Y. Chen, “Improving resolution of second harmonic generation microscopy via scanning structured illumination,” Biomed. Opt. Express **9**(12), 6081–6090 (2018).
29. L. Gong and H. Wang, “Breaking the diffraction limit by saturation in stimulated-Raman-scattering microscopy: A theoretical study,” Phys. Rev. A **90**(1), 013818 (2014).
30. Y. Yonemaru, A. F. Palonpon, S. Kawano, N. I. Smith, S. Kawata, and K. Fujita, “Super-spatial- and -spectral-resolution in vibrational imaging via saturated coherent anti-stokes Raman scattering,” Phys. Rev. Appl. **4**(1), 014010 (2015).
31. S. Rieger, M. Fischedick, K. J. Boller, and C. Fallnich, “Suppression of resonance Raman scattering via ground state depletion towards sub-diffraction-limited label-free microscopy,” Opt. Express **24**(18), 20745–20754 (2016).
32. W. R. Silva, C. T. Graefe, and R. R. Frontiera, “Toward Label-Free Super-Resolution Microscopy,” ACS Photonics **3**(1), 79–86 (2016).
33. L. Gong, W. Zheng, Y. Ma, and Z. Huang, “Saturated Stimulated-Raman-Scattering Microscopy for Far-Field Superresolution Vibrational Imaging,” Phys. Rev. Appl. **11**(3), 034041 (2019).
34. Z. Li, K. Aleshire, M. Kuno, and G. V. Hartland, “Super-resolution far-field infrared imaging by photothermal heterodyne imaging,” J. Phys. Chem. B **121**(37), 8838–8846 (2017).
35. J. Shi, T. T. Wong, Y. He, L. Li, R. Zhang, C. S. Yung, J. Hwang, K. Maslov, and L. V. Wang, “High-resolution, high-contrast mid-infrared imaging of fresh biological samples with ultraviolet-localized photoacoustic microscopy,” Nat. Photonics **13**(9), 609–615 (2019).
36. H. Wang, Q. Xie, and X. G. Xu, “Super-Resolution Mid-Infrared Spectro-Microscopy of Biological Applications through Tapping Mode and Peak Force Tapping Mode Atomic Force Microscope,” Adv. Drug Delivery Rev. **180**, 114080 (2022).

37. C. Wang, T. Zhang, and W. Wang, “Design method for an aspheric Schwarzschild objective with a low obscuration and an infinite conjugate distance,” Opt. Commun. **460**, 125055 (2020).
38. R. E. Izzaty, B. Astuti, and N. Cholimah, “Pluto-2 Manual,” https://holoeye.com/slm-pluto-phase-only/.
39. K.M. Mohammad, A. M. Choubal, and Jr. K. C. Toussaint, “Application of a reflective microscope objective for multiphoton microscopy,” J. Microsc. **271**(2), 129–135 (2018).
40. H. Inagawa, Y. Toratani, K. Motohashi, I. Nakamura, M. Matsushita, and S. Fujiyoshi, “Reflecting microscope system with a 0.99 numerical aperture designed for three-dimensional fluorescence imaging of individual molecules at cryogenic temperatures,” Sci. Rep. **5**(1), 1–5 (2015).
41. R. W. Boyd, *Nonlinear Optics*, (Academic, 2020).
42. Y. Xiao, Z. Yu, R. A. Wambold, H. Mei, G. Hickman, R. H. Goldsmith, M. Saffman, and M. A Kats, “Efficient generation of optical bottle beams,” Nanophotonics **10**(11), 2893–2901 (2021).
43. V. V. Krishnamachari and E. O. Potma, “Multi-dimensional differential imaging with FE-CARS microscopy,” Vib. Spectrosc. **50**(1), 10–14 (2009).
44. J. X. Cheng and X. S. Xie, “Green’s function formulation for third-harmonic generation microscopy,” J. Opt. Soc. Am. B **19**(7), 1604–1610 (2002).
45. S. S. Wang and R. Magnusson, “Theory and applications of guided-mode resonance filters,” Appl. Opt. **32**(14), 2606–2613 (1993).
46. H. Li, K. F. Kelly, and S. Baldelli, “Spectroscopic imaging of surfaces - Sum frequency generation microscopy (SFGM) combined with compressive sensing (CS) technique,” J. Chem. Phys. **153**(19), 190901 (2020).
47. L. Zhou, H. Fu, T. Lv, C. Wang, H. Gao, D. Li, L. Deng, and W. Xiong, “Nonlinear optical characterization of 2d materials,” Nanomaterials **10**(11), 2263 (2020).
48. R. Biswas, M Dandu, S. Menon, K. K. Jha, K. M. Jyothsna, K. Majumdar, and V. Raghunathan, “Third harmonic generation in multilayer Tin Diselenide under the influence of Fabry-Perot interfence effects,” Opt. Express **27**(20), 28855–28865 (2019).
49. R. Biswas, M. Dandu, A. Prosad, S. Das, S. Menon, J. Deka, K. Majumdar, and V. Raghunathan, “Strong near band-edge excited second-harmonic generation from multilayer 2H Tin diselenide,” Sci Rep **11**(1), 15017 (2021).